



POLITECNICO
MILANO 1863

RE.PUBLIC@POLIMI

Research Publications at Politecnico di Milano

Post-Print

This is the accepted version of:

F. Maggi

Curing Viscosity of HTPB-Based Binder Embedding Micro and Nano-Aluminum Particles
Propellants, Explosives, Pyrotechnics, Vol. 39, N. 5, 2014, p. 755-760
doi:10.1002/prop.201400010

The final publication is available at <https://doi.org/10.1002/prop.201400010>

Access to the published version may require subscription.

This is the peer reviewed version of the following article: Curing Viscosity of HTPB-Based Binder Embedding Micro and Nano-Aluminum Particles, which has been published in final form at <https://doi.org/10.1002/prop.201400010>. This article may be used for non-commercial purposes in accordance with Wiley Terms and Conditions for Use of Self-Archived Versions.

When citing this work, cite the original published paper.

Permanent link to this version

<http://hdl.handle.net/11311/844537>

Curing viscosity of HTPB-based binder embedding micro- and nano-aluminum particles

Filippo Maggi*^[a]

Abstract: Aluminum is used as a metal fuel in energetic materials for the improvement of propulsion performance and density. Both nano-sized and micron-sized activated powders represent valuable options in order to improve metal combustion properties, each possessing advantages and drawbacks. These ingredients bear peculiar properties (namely, higher specific surface, coatings, or surface characteristics) which generate high mixing viscosity once suspended in a polymer as well as altered mechanical properties of the final product. The present work takes into consideration four different powders dispersed in a polymer binder and investigates the evolution of viscosity in time during the curing process. The suspending medium is represented by a mixture of hydroxyl-terminated polybutadiene (HTPB), isophorone diisocyanate (IPDI) and dioctyl adipate (DOA). Viscosity was measured for 5 hours on samples under isothermal curing at 60°C. Non-isothermal DSC kinetic analyses were also performed using the Kissinger method. It was found that, for the test conditions, a size reduction of metal particles slowed down the increment rate of curing viscosity while some peculiar coatings, such as fatty acids, introduced opposite trends.

Keywords: aluminum particles, viscosity, nanometric, micrometric, HTPB

1 Introduction

Aluminum, in the shape of micrometric particles ranging from 5 to 50 μm , represents a standard fuel for space launcher applications, being a good compromise between performance improvements, stability in time, cost, low toxicity, and availability [1]. The agglomeration attitude of these metal particles, on the burning surface, is the cause of condensed phase combustion products which are responsible for specific impulse losses due to two-phase flow nozzle expansion [2,3]. Advanced aluminum powders featuring improved reactivity aimed at easier particle ignition were and are currently developed as an answer to the need for better combustion properties [4-7].

The use of nano-sized particles in the range 50-200 nm is justified by lower ignition temperature, faster propellant burning rates, and thin flaky aggregates. The main drawbacks consist of reduced metal content, high moisture sensitivity, increased mixing viscosity, and influence on the mechanical properties of the final product [8-12]. Coatings of fatty acids (generally, stearic or palmitic), polymers, or other chemicals may be applied to the particle surface to prevent further environmental degradation or to ease dispersion [13,14]. Modeling and experimental methods to investigate nanoparticle mixing were recently published by Reese and co-authors [15].

Micron-sized particles with specific surface activations grant some reactivity benefits, but are also easier to handle and mix, with lower expected cost, and higher effective metal content. Conversely, their processing may lead to the modification of the surface composition and finishing as well as a change in the shape factor, which eventually favors higher mixing viscosity [16-19].

Hydroxyl-terminated polybutadiene (HTPB) is

a typical pre-polymer widely used in propellant formulations. The curing kinetics of the HTPB binder depends on the reciprocal concentration of NCO and OH groups. The isothermal viscosity level relates to the growth of the average molecular weight of the polymer chains and typically follows an exponential trend in the shape $\eta(t) = \eta_0 \exp(k_1 t)$ [20]. It has been observed that the solids loading has a significant effect on the process [21,22]. Papers relevant to the connection between curing viscosity and filler type were not retrieved in the open literature by the author.

The present paper addresses the isothermal viscosity of metalized HTPB-based binders filled with four different types of metal powders: two nanometric and two micrometric. The solid loading was limited to a 10% fraction by mass (about 4% by volume) in order to reduce particle-particle interaction. These formulations were not meant to be representative of optimized energetic materials characterized by higher solid loading, such as solid propellants, but were formulated to give a perspective on binder reactivity. Complex viscosity build-up in time was measured using a flat-plate rheometer in a strain-controlled oscillatory test for five hours at 60°C. Model-free curing kinetics of selected mixes were also investigated using DSC and the Kissinger method.

2 Materials

2.1 Powders and additives

The powders used in this work were characterized as part of the European FP7 project HISP (High performance solid propellants for In-Space Propulsion) and details on their physical as well as combustion properties can be found in previous works of the same research group [6,7]. A summary of nominal size, mass-mean diameter $d[4,3]$, specific surface area S_a , and active aluminum content is reported in Table 1.

[a] *F. Maggi*
Politecnico di Milano
Dept. of Aerospace Science and Technology
Space Propulsion Laboratory
Via La Masa 34, 20156 Milan, MI, Italy
E-mail: filippo.maggi@polimi.it

Table 1. Properties of tested aluminum powders. The Al₀ fraction was quantified through hydrolysis; the procedure is described in [7]; confidence interval is 95%. (*: nominal data from supplier)

	Nom. Size μm	d[4,3] μm	S _a , m ² /g	Al ₀ , %
μAl-18	4.5	5.1	1.2	98.3±0.7
aAl-19a	4.5	5.4	2.6	93.9±0.6
nAl-01i	0.1	0.141	13.5	88.7±0.2
nAl-07e	0.1	0.149	10.5	91.6±1.1
Al ₂ O ₃	<10	8.2	N.Av.	<0.5*
AlF ₃	N.Av.	20.9	N.Av.	<0.5*

The μAl-18 powder (producer Valimet Inc., type H3) is nearly spherical with a smooth surface, naturally covered by an oxide layer.

The aAl-19a powder, shown in Figure 1, was derived from the μAl-18 batch with a process of chemical activation through a fluorine-based solution. The surface of the powder is rough after the treatment, granting a higher specific surface without altering its shape factor. The powder particle size was minimally increased by 0.3 μm. Powder processing was performed at FOI, using a method developed by Hahma [16]. The surface atomic concentration, analyzed through XPS, consisted of 58% of oxygen, 5.5% of carbon, 13% of fluorine, and 17% of aluminum in the oxidized state +3. Traces of boron (3%), potassium (1.5%), and manganese (2.1%) were identified as well. The simultaneous presence of both AlF₃ and Al₂O₃ is possible owing to detected relative concentrations.

Other compositions were formulated aiming at a better understanding of the effects introduced by these modified aluminum powders on binder curing. The metal fuel was totally replaced with aluminum oxide (alpha phase, measured d[4,3]=8.2 μm, Sigma Aldrich, lot MKBJ1604C) and aluminum fluoride (rhombohedral alpha phase, measured d[4,3]=20.9 μm, Sigma Aldrich, lot MKBP1432V), maintaining the volumetric filling factor of the initial metalized composition. Tests with pure binder and carboxyl acids were performed as well (palmitic acid lot SZBD1970V, stearic acid lot MKBM0661V, both supplied by Sigma Aldrich).

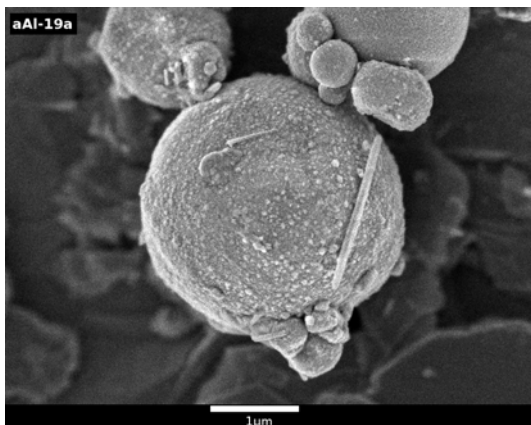


Figure 1. SEM micrograph of micro-aluminum aAl-19a (magnification 20k)

The uncoated nanoaluminum powder nAl-01i was produced using the EEW technique and was supplied by Sibthermochim (commercial name ALEXTM). The particles were spherical, smooth, and naturally covered by a passivation layer of aluminum oxide. The particle size, measured by laser granulometry using wet dispersion, was 0.141 μm.

The nAl-07e powder is a nanoaluminum whose commercial name is L-ALEXTM. It is produced by coating the surface of nAl-01i with a carboxyl acid (stearic or palmitic) to prevent further material degradation after the exposure to air and moisture. The specific melting peak of the palmitic acid coating was identified by DSC in this batch. Its mass-mean diameter was 0.149 μm, as determined by granulometry using wet dispersion.

2.2 Suspending medium

The suspending medium consisted of an HTPB-R45 oligomer by Cray Valley (lot V1501B, hydroxyl value 0.83±0.05 meqKOH/g, molar mass 2800 g/mol) mixed with IPDI, using an NCO:OH ratio of 1.04. The mass fractions of DOA and of the aluminum fuel were 13% and 10% respectively. Batches of 5 grams were mixed with a Resodyn Labram resonant mixer at about 50 g acceleration for 5 minutes under vacuum (15 kPa absolute pressure). The vessel was air-cooled to ambient temperature (21±2 °C), in order to prevent temperature rise from mixing, with a specific in-house device.

3 Experimental Section

The mixed samples were tested on a flat-plate rheometer (TA AR2000ex) at 60°C constant temperature. A thermal stabilization of 5 minutes was applied before starting the measurement. Complex viscosity $|\eta^*|$ was mapped during a 5-hour-long test with a 2% strain-controlled procedure under a reference frequency of 1 Hz. The strain was selected in order to operate in the linear field. The real component η' of the complex viscosity (in-phase viscosity) was observed to be much higher than the imaginary part η'' (out-of-phase viscosity, elastic behavior) for tested mixes, with the exception of samples containing a carboxyl acid. In the latter case, the suspensions approached or even crossed the gel point during the 5-hour tests, being the gel point identified by the relation $\eta' = \eta''$ [23].

Model-free apparent curing kinetics for selected mixes were investigated using the Kissinger non-isothermal method. Differential scanning calorimeter (DSC) tests were conducted at heating rates of 2.5, 5, 10, 20 K/min over the range of -20°C to 300°C on a TA 2010 DSC instrument using argon as purging gas (purity >99.995%). The activation energy (E_a) and pre-exponential factor (A) were fitted through Eq. (1) [22].

$$\ln(\beta / T_p^2) = \ln(AR / E_a) - E_a / (RT_p) \quad (1)$$

4 Results

A summary of the results obtained for the binder-fuel suspensions is given in Table 2. The isothermal build-up in time of $|\eta^*|$ is reported for all mixtures per each hour of processing, starting from the beginning of the test, after five minutes of thermal stabilization.

Table 2. Time evolution of isothermal viscosity $|\eta^*|$ for fuel-binder suspensions.

Time min	0	60	120	180	240	300
No add.	0.560	0.776	1.074	1.472	1.981	2.693
μ Al-18	0.579	0.756	0.960	1.241	1.554	1.962
aAl-19a	0.609	0.760	0.962	1.199	1.506	1.909
nAl-01i	0.854	0.936	1.108	1.383	1.714	2.134
nAl-07e	0.855	1.259	1.941	2.875	4.178	6.083
Al_2O_3	0.642	0.947	1.355	1.946	2.793	4.033
AlF_3	0.896	1.192	1.608	2.176	3.011	4.177
Palmitic	0.817	3.501	13.46	65.27	Gelled in 230 min	
Stearic	0.824	4.020	19.45	111.4	Gelled in 218 min	

4.1 Initial viscosity

The suspensions behaved like a Newtonian fluid under the conditions of the test. This was also observed by Teipel and Förter-Barth [24]. The initial isothermal viscosity $|\eta^*|$ of the mixtures increased as the specific surface area of the filler increased. The slurries filled with nanometric particles had about 50 percent higher initial viscosity than the micrometric filled samples. The mixture filled with μ Al-18 aluminum had the lowest initial viscosity. These findings are similar to those of Teipel and Förter-Barth [24] and Roscoe [25] for the nanometric based samples and Arefinia and Shojaei [25] for micron-sized powders. Based on mere size considerations, the aAl-19a and μ Al-18 can be classified as dilution fillers which contribute to viscosity mainly through hydrodynamic effects. The aluminum oxide and the aluminum fluoride also belong to this category. The viscosity of Al_2O_3 suspension was comparable to the one produced by μ Al-18, owing to similar particle size of the fillers. The higher initial viscosity of AlF_3 mixes was attributed to a different particle shape. The nAl-01i and nAl-07e powders are semi-reinforcing fillers producing particle-to-particle interaction despite the limited solids loading [26]. A high initial viscosity of polymers mixed with carboxyl acids resulted in fast curing reactions during the pre-test conditioning phase.

The aAl-19a and μ Al-18 powders have the same shape factor and almost identical particle size. The diameter of the aAl-19a powder, $D[4,3]$, increased by 0.3 μ m and an external roughness was formed due to some deposits derived from activation of the surface. Despite its more-than-doubled specific surface area, the effect on compound viscosity was only +5%, when compared to μ Al-18. This small amount may be explained by the fact that specific surface was increased by an alteration of the particle

superficial finishing, and not by the variation of shape or size. Discussions on this point are not abundant in the literature although some authors have addressed the matter. Macro-scale experiments on cements conducted by Erdoğan *et al.* did not show appreciable effects on viscosity generated by the level of superficial finishing of suspended particles for different filling factors [27]. The problem was addressed theoretically by Wilson and Davis, who found a negative contribution to the global viscosity, proportional to the square of the volume concentration [28]. The effect was negligible for suspensions with low filling factors or high roughness height and was surpassed by the effect of variation of the apparent particle diameter, which is a function of the superficial roughness of the particles.

The size and shape of the nAl-07e resembles that of nAl-01i, in the nanoaluminum group. The organic coating is expected to ease dispersion in a polymer matrix but it also reduces the specific surface area about 25% without appreciable influence on the compound viscosity. Similar results were found by Mary and co-authors on HDPE-coated nanoaluminum suspended in HTPB for comparable low volumetric fractions [13].

4.2 Temporal evolution of viscosity

Table 3 summarizes the parameters of the exponential function $|\eta^*| = |\eta^*|_0 \exp(k_\eta t)$ fitted to the experimental viscosity data. The constant $|\eta^*|_0$ represents the intercept at time $t = 0$, while k_η is the rate constant for the viscosity increment in time. The statistical correlation parameter R^2 is above 0.99 for all cases. Data are presented for both metal-polymer suspensions and for additional supporting analyses.

Table 3. Exponential fitting of isothermal viscosity build-up $|\eta^*| = |\eta^*|_0 \exp(k_\eta t)$.

	$ \eta^* _0$ Pa·s	k_η 1/min	R^2
No add.	0.561	0.00527	0.9994
μ Al-18	0.587	0.00407	0.9992
aAl-19a	0.598	0.00387	0.9993
nAl-01i	0.768	0.00332	0.9923
nAl-07e	0.852	0.00665	0.9989
Al_2O_3	0.654	0.00604	0.9999
AlF_3	0.862	0.00520	0.9995
Palmitic	0.791	0.02421	0.9989
Stearic	0.789	0.02700	0.9992

The slowest viscosity buildup rate was obtained for compositions containing the uncoated nanoaluminum nAl-01i. Higher rates were found for aAl-19a and μ Al-18, respectively, although the resulting k_η was still lower than the baseline polymer. The suspension containing the coated nAl-07e, in contrast, exhibited a doubled rate as compared to the uncoated nanoaluminum, and was about 20% higher than the baseline formulation.

The rate constant for aluminum oxide suspensions was found to be higher than that of the baseline composition while about the same value was found for mixtures containing aluminum fluoride. Tests performed to investigate the influence of fatty acids on the curing process showed increased kinetics, resulting in a rate constant k_n five times higher than the baseline suspension. These analyses were conducted without metal fuel, by dispersing the fatty acid in the HTPB pre-polymer. The additive mimicked the amount of the coating introduced by the nAl-07e powder. The weight of the protective layer was assumed to be the 5% of the whole particle mass, in compliance with Teipel's assertion [29].

4.3 Curing kinetics

Non-isothermal DSC analyses were performed on selected suspensions. Micrometric and nanometric uncoated aluminum (μ Al-18 and nAl-01i), coated nanoaluminum (nAl-07e) and aluminum oxide were investigated. Peak reaction temperature and Arrhenius parameters derived by the Kissinger method are reported in Table 4.

Table 4. Non-isothermal DSC peaks and fitting parameters for model-free curing kinetics.

	No add.	μ Al-18	nAl-01i	nAl-07e	Al ₂ O ₃
T_p ($\beta = 2.5$ K / min)	168.3	166.0	167.9	152.8	166.4
T_p ($\beta = 5$ K / min)	179.9	174.7	175.9	161.6	177.9
T_p ($\beta = 10$ K / min)	187.5	189.3	188.9	172.9	188.9
T_p ($\beta = 20$ K / min)	201.6	203.1	202.6	181.6	201.8
A	114.3	17.0	42.1	121.6	40.8
E_a	14.97	12.25	13.54	13.53	13.49
R ²	0.987	0.992	0.992	0.994	0.999

The activation energies were similar for all the tested compounds, regardless of the particle size or the presence of a fatty acid coating. The highest and the lowest values were obtained for the baseline binder (14.97 kJ/mol) and for the suspension embedding μ Al-18 (12.25 kJ/mol) respectively. Some differences were observed in the pre-exponent. The value of the parameter A for all uncoated metal slurries as well as Al₂O₃ suspensions was at least 5 times lower than the value obtained for the nAl-07e mix and the pure binder.

5 Discussion

All of the aluminum suspensions, with the exception of the nAl-07e mixture, resulted in a reduced viscosity build-up rate, when compared to the unloaded HTPB-based polymer. The presence of uncoated metal particles inside the polymer caused a dampening effect on the curing kinetics, resulting in a progressive decrease of the k_n parameter. A stronger reduction was obtained for the mixtures containing powders with a higher specific surface area. The fact that a micrometric filler can slow down the HTPB viscosity increment was acknowledged by Mahanta

and Pathak [22]. Another confirmation can be found in a report by McManus *et al.*, where the authors scrutinized the effect on binder curing by different propellant ingredients [30]. Kinetic tests for the specific case of aluminum were reported for different micrometric powders finding that the relative curing reaction rate increased when using particles characterized by larger diameter. The kinetic tests performed in the present work on uncoated aluminum slurries confirmed the dampening effect with respect to the baseline binder but also noted that the trend did not extend into the nanometric range.

The curing of the Al₂O₃ suspension featured a viscosity build-up rate almost double that of the aluminized compositions. Alumina is known to increment the polymerization rate in other polyaddition processes, such as the epoxy-amine reactions [31]. However, no peculiar behavior was observed from a kinetic standpoint. It should be noted that all uncoated metal particles are covered by a natural layer of amorphous aluminum oxide which might behave in a different way with respect to the alpha phase of the tested Al₂O₃ additive. A definitive explanation for the dampening effect is not yet available and is beyond the scope of this paper, however, both mobility depression of the molecular chains by the filler and more complex chemical interactions with the suspended particles cannot be excluded.

Surface particle treatment of the μ Al-19a did not produce significant modifications of the curing reaction with respect to the original μ Al-18 powder, limiting its action on a variation of the initial viscosity. The tests on suspensions of AlF₃, present on the activated surface, did not demonstrate peculiar behavior. The rate constant k_n was similar to the one observed by the baseline polymer, owing to the fact that the AlF₃ additive was relatively coarse.

Interesting properties were shown by ALEX nano-powders. The dampening effect on the curing rate of the uncoated nAl-01i was the strongest. The presence of an organic layer on the surface of nAl-07e did not contribute to the reduction of the initial mixing viscosity but delivered higher $[\eta^*]$ increment rate. Also the kinetic pre-exponential parameter was higher with respect to the other metal powders. Such behavior may be attributed to the presence of the acid-kind protective coating. Baseline compositions embedding palmitic or stearic acids demonstrated a substantial increase in the reaction rate, with no difference between the two materials. The result was expected, since it is known from organic chemistry that carboxyl acids react with NCO groups of isocyanate forming amides. However, further reactivity with the aluminum carboxylate, present at the first atomic layer of the coated particle, might also be possible [33,34].

6 Conclusion

This paper addressed the isothermal viscosity buildup of a HTPB-based binder embedding micron- and nano-sized particles with different surface treatments. The analysis showed that, under the tested

conditions, metal-polymer curing kinetics was reduced using uncoated aluminum powders. Particle size was observed to play a role in this respect finding a slower reaction rate for higher specific surface area. The origin for this effect, observed for both nanometric and micrometric powders, has not been yet fully understood. Both mobility depression of the molecular chains by the filler and more complex chemical interactions with the suspending material cannot be excluded so far. A high viscosity level and development rate was observed for the nanoaluminum coated with fatty acid resulting in a final value three times higher than the uncoated variant. Reaction between isocyanate and fatty acid, or isocyanate and carboxylate product of the coating process, is the possible reason. Finally, it should be underlined that results were retrieved under a condition of low filler volume fraction, in order to minimize the particle-particle interaction effect. Extrapolation to highly loaded compositions, typical of propellants, might not be straightforward.

Symbols

A Arrhenius pre-exponential factor, 1/s
 $d_{[4,3]}$ Mass-weighted mean diameter, μm
 E_a Arrhenius activation energy, kJ/mol
 k_n Rate constant for viscosity buildup, 1/s
 R Universal gas constant, 8.314 J/(mol K)
 R^2 Coefficient of determination
 S_a Specific surface area, m^2/g
 t Time, s (if not differently stated)
 T_p Peak temperature, K
 x', x'', x^* Real, imaginary and complex value of x
 $|x|$ Modulus of x
 β Heating rate, K/s (if not differently stated)
 η Viscosity, Pa·s

Abbreviations

Al_0 Active aluminum content
 aAl Activated aluminum
 BET Brunauer-Emmet-Teller
 DOA Dioctyl adipate
 DSC Differential scanning calorimeter
 EEW Electrical explosion of wires
 FOI Swedish Defense Research Agency
 HDPE High density polyethylene
 HTPB Hydroxyl-terminated polybutadiene
 IPDI Isophorone diisocyanate
 nAl Nano-sized aluminum
 No Add. Baseline formulation
 SEM Scanning electron microscopy
 XPS X-ray photoelectron spectroscopy
 μAl Micron-sized aluminum

Acknowledgements

This work was partially funded by the European FP7 Project HISP (High performance solid propellants for In-Space Propulsion), Grant Agreement No. 262099. The author acknowledges the work of Istituto ENI Donegani, Novara, Italy for SEM and BET analysis, as well as Prof. G. Sala, Prof. L. Di Landro ,

Prof. F. Severini, Ms. L. Meda, and Mr. G. Marra for instrumentation availability and fruitful discussions. Finally, the author wishes to acknowledge the work of Alice Atwood who kindly revised the script for English polishing.

References

- [1] J. P. Sutton, O. Biblarz, *Rocket Propulsion Elements*, Seventh ed., Wiley, New York, NY, USA, **2001**.
- [2] F. Maggi, A. Bandera, L. Galfetti, L. T. DeLuca, T. L. Jackson, Efficient Solid Rocket Propulsion for Access to Space, *Acta Astronaut.* **2010**, *66*, 1563–1573.
- [3] D. Reydellet, *Performance of Rocket Motors with Metallized Propellants*, Advisory Report AR-230, Advisory Group for Aerospace Research and Development (AGARD), **1986**.
- [4] L. T. DeLuca, L. Galfetti, F. Maggi, G. Colombo, A. Reina, S. Dossi, D. Consonni, M. Brambilla, Innovative Metallized Formulations for Solid Rocket Propulsion, *Chin. J. Energ. Mater.* **2012**, *20*, 465-474.
- [5] L. T. DeLuca, E. Marchesi, M. Spreafico, A. Reina, F. Maggi, L. Rossetini, A. Bandera, G. Colombo, B. M. Kosowski, Aggregation Versus Agglomeration in Metallized Solid Rocket Propellants, *Int. J. Energ. Mater. Chem. Propuls.* **2010**, *9*, 91-105.
- [6] S. Dossi, A. Reina, F. Maggi, L. T. De Luca, Innovative Metal Fuels for Solid Rocket Propulsion, *Int. J. Energ. Mater. Chem. Propuls.* **2012**, *11*, 299–322.
- [7] F. Maggi, S. Dossi, A. Reina, M. Fassina, L. T. De Luca, Advanced Aluminum Powders for Solid Propellants, *5th European Conference for Aerospace Sciences (EUCASS 2013)*, Munich, Germany, 1-5 July, **2013**.
- [8] A. Dokhan, E. W. Price, J. M. Seitzman, R. K. Sigman, The Ignition of Ultra-Fine Aluminum in Ammonium Perchlorate Solid Propellant Flames, *AIAA Paper 2003-4810*, *39th AIAA/ASME/SAE/ASEE Joint Propulsion Conference and Exhibit*, Huntsville, AL, 20-23 July, **2003**.
- [9] L. Galfetti, F. Severini, L. T. DeLuca, G. Marra, L. Meda, R. Braglia, Ballistics and Condensed Combustion Residues of Aluminized Solid Rocket Propellants, *Proceedings of 9-IWCP, International Workshop on Novel Energetic Materials and Applications*, (L. T. DeLuca, L. Galfetti, R. A. Pesce-Rodriguez, Eds.), La Spezia, Italy, 14-18 September, **2004**.
- [10] E. M. Popenko, A. A. Gromov, Y. Y. Shamina, A. V. Sergienko, N. I. Popok, Effect of the Addition of Ultrafine Aluminum Powders on the Rheological Properties and Burning Rate of Energetic Condensed Systems, *Combust. Explos. Shock Waves* **2007**, *43*, 46–50.

- [11] E. L. Dreizin, Metal-based Reactive Nanomaterials, *Prog. Energy Combust. Sci.* **2009**, *35*, 141–167.
- [12] J. Bouillard, A. Vignes, O. Dufaud, L. Perrin, D. Thomas, Ignition and Explosion Risks of Nanopowders, *J. Hazard. Mater.* **2010**, *181*, 873–880.
- [13] B. Mary, C. Dubois, P. J. Carreau, P. Brousseau, Rheological Properties of Suspensions of Polyethylene-coated Aluminum Nanoparticles, *Rheol. Acta* **2006**, *45*, 561–573.
- [14] A. Reina, Nano-metal Fuels for Hybrid and Solid Propulsion, *PhD Thesis*, Politecnico di Milano, Milan, Italy, 2013.
- [15] D. A. Reese, S. S. Son, N. M. Lačević, D. L. Naud, Improvements in Nanoparticle Dispersion Methods for Solid Propellants, *AIAA Paper 2010-6662*, 46th AIAA/ASME/SAE/ASEE Joint Propulsion Conference and Exhibit, Nashville, TN, 25-28 July, **2010**.
- [16] A. Hahma, A. Gany, K. Palovuori, Combustion of activated aluminum, *Combust. Flame* **2006**, *145*, 464–480.
- [17] S. Dossi, F. Maggi, L. Facciolati, L. T. DeLuca, Activation of Micrometric Aluminum - Metal Oxide Mixtures by Mechanical Milling, *5th European Conference for Aerospace Sciences (EUCASS 2013)*, Munich, Germany, 1-5 July, **2013**.
- [18] T. R. Sippel, S. F. Son, L. J. Groven, Altering Reactivity of Aluminum with Selective Inclusion of Polytetrafluoroethylene through Mechanical Activation, *Propellants Explos. Pyrotech.* **2013**, *38*, 286–295.
- [19] T. R. Sippel, S. F. Son, L. J. Groven, Aluminum Agglomeration Reduction in a Composite Propellant Using Tailored Al/PTFE Particles, *Combust. Flame* **2014**, *161*, 311–321.
- [20] A. H. Navarchian, F. Picchioni, L. P. B. M. Janssen, Rheokinetics and Effect of Shear Rate on the Kinetics of Linear Polyurethane Formation, *Polym. Eng. Sci.* **2005**, *45*, 279–287.
- [21] R. M. Muthiah, V. N. Krishnamurthy, B. R. Gupta, Rheology of HTPB Propellant: Development of Generalized Correlation and Evaluation of Pot Life, *Propellants Explos. Pyrotech.* **1996**, *21*, 186–192.
- [22] A. K. Mahanta, D. D. Pathak, HTPB-Polyurethane: A Versatile Fuel Binder for Composite Solid Propellant, in: *Polyurethane*, (F. Zafar, E. Sharmin, Eds.), InTech, Rijeka, Croatia, **2012**.
- [23] H. H. Winter, Can the Gel Point of a Cross-Linking Polymer Be Detected by the G'–G'' Crossover?, *Polym. Eng. Sci.* **1987**, *27*, 1698–1702.
- [24] U. Teipel, U. Förter-Barth, Rheology of Nano-Scale Aluminum Suspensions, *Propellants Explos. Pyrotech.* **2001**, *26*, 268–272.
- [25] R. Roscoe, The Viscosity of Suspensions of Rigid Spheres, *Br. J. Appl. Phys.* **1952**, *3*, 267.
- R. Arefinia, A. Shojaei, On the Viscosity of Composite Suspensions of Aluminum and Ammonium Perchlorate Particles Dispersed in Hydroxyl Terminated Polybutadiene. New Empirical Model, *J. Colloid Interface Sci.* **2006**, *299*, 962–971.
- [26] J. L. Leblanc, Rubber–Filler Interactions and Rheological Properties in Filled Compounds, *Prog. Polym. Sci.* **2002**, *27*, 627–687.
- [27] S. T. Erdoğan, N. S. Martys, C. F. Ferraris, D. W. Fowler, Influence of the Shape and Roughness of Inclusions on the Rheological Properties of a Cementitious Suspension, *Cem. Concr. Compos.* **2008**, *30*, 393–402.
- [28] H. J. Wilson, R. H. Davis. The Viscosity of a Dilute Suspension of Rough Spheres, *J. Fluid Mech.* **2000**, *421*, 339–367.
- [29] U. Teipel, John Wiley & Sons. *Energetic Materials: Particle Processing and Characterization*, Wiley-VCH, Weinheim, **2005**.
- [30] S. P. McManus, H. S. Bruner, H. D. Coble, Stabilization of Cure Rates of Diisocyanates with Hydroxy-Terminated Polybutadiene Binders, *Research Report 140*, University of Alabama in Huntsville, **1973**.
- [31] R. Sanctuary, J. Baller, B. Zielinski, N. Becker, J. K. Krüger, M. Philipp, U. Müller, M. Ziehmer, Influence of Al₂O₃ Nanoparticles on the Isothermal Cure of an Epoxy Resin, *J. Phys. Condens. Matter* **2009**, *21*, 035118, 1-8.
- [32] W. J. Blank, Z. A. He, E. T. Hessell, Catalysis of the Isocyanate-Hydroxyl Reaction by Non-Tin Catalysts, *Prog. Org. Coat.* **1999**, *35*, 19–29.
- [33] M. Cliff, F. Tepper, V. Lisetski, Ageing Characteristics of ALEX Nanosize Aluminum, *AIAA Paper 2001-3287*, 37th AIAA/ASME/SAE/ASEE Joint Propulsion Conference and Exhibit, Salt Lake City, UT, USA, 8-11 July, **2001**

DSMC Simulation of Rarefied Gas Mixtures Flows past Arrays of Absorbing Plates

Aldo Frezzotti, Gian Pietro Ghiroldi, Livio Gibelli

*Politecnico di Milano, Dipartimento di Scienze & Tecnologie Aerospaziali
Via La Masa, 34 - 20156 Milano, Italy*

Antonio Bonucci

*SAES Group
Viale Italia 77 - 20020 Lainate - Italy*

Abstract

Gas flows induced by arrays of absorbing surfaces of various shapes are met in several vacuum technology devices, like NEG or cryogenic pumps. In order to obtain a simplified model of low pressure gas dynamics driven by surface absorption, flows of rarefied gas binary mixtures past arrays of absorbing plates are studied by numerical solution of a system of coupled and spatially two-dimensional Boltzmann equations. The overall absorption rate is obtained as a function of problem parameters which include the characteristic flow Knudsen number and wall absorption probabilities. Particular attention is devoted to mixtures flows in which one of the components is present in small amounts and it is weakly absorbed.

Keywords: Rarefied gases, mixtures, surface absorption, condensation

1. Introduction

In a previous paper[1], the authors have studied one-dimensional steady flows of binary gas mixtures in contact with an infinite planar wall which absorbs the two gas components at different rates. Flow properties have been investigated by solving a system of two coupled Boltzmann equations[2, 3], since the proper formulation of boundary conditions and the presence of a Knudsen layer above the absorbing plates require kinetic theory concepts and methods. It has been observed that the one-dimensional steady absorption problem is virtually equivalent to a classical condensation problem[4, 5, 6] and that the presence of a small amount of a weakly absorbed component can significantly affect the absorption rate of the most abundant species, in complete analogy with similar results about condensation flows[7].

Although many flow properties can be understood by the study of the one-dimensional problem, the geometry considered in Ref.[1] is far from the complex

shapes present in vacuum technology devices, like NEG or cryogenic pumps[8], in which absorbing surfaces are organized in more or less densely packed arrays. Gas flow properties in general and absorption rates in particular are then expected to be affected not only by gas-wall and mixture components interactions but also by devices geometry. In order to obtain a more precise description of the dynamics of low pressure gas mixtures flows in vacuum devices, in this paper we address the numerical computation of the two-dimensional steady solution of a system of two-coupled Boltzmann equations for a binary mixture of hard sphere gases[3]. Gas flows are generated by the presence of absorbing surfaces arranged in an infinite array of identical and parallel plates. As shown below, the solutions of the problem are determined by a relatively large number of physical and geometrical parameters. Hence attention has been mainly focused on two aspects of the problem. The first one is the assessment of the effects of the degree of gas rarefaction (defined through a characteristic flow Knudsen number [2]) on the overall absorption rate. The second one is the effect of the interaction of the two components of a binary mixture on the absorption rate. In particular, the situation has been investigated in which one of the components is present in small amounts and is weakly absorbed by the array plates. As mentioned above, in a one-dimensional model the presence of a species with small absorption probability can considerably decrease the overall mixture absorption rate. However, the flow geometry is expected to play a role and its influence needs to be investigated. Accordingly, the paper is organized as follows: Sections 2 and 3 present the mathematical formulation and briefly describe the adopted numerical method; section 4 presents and discusses collision-less solutions of the Boltzmann equation which describe high vacuum operation of the absorbing surfaces array. Moreover, they provide reference conditions to judge about the device performances in the transition regime[2] discussed in section 5, which presents the results of single component gas flows at different degrees of rarefaction as well as selected properties of binary mixtures flows. Results are finally summarized in the concluding section 6.

2. Problem formulation

In the problem considered here, a binary mixture of monatomic hard sphere gases occupies an infinite spatial region. The atoms of species i ($i = 1, 2$) have mass m_i and hard sphere diameter σ_i . It is assumed that the mixture stationary motion is governed by a system of two coupled, steady Boltzmann equations[3] in the form:

$$\mathbf{v} \circ \frac{\partial f_i}{\partial \mathbf{r}} = \sum_{j=1}^2 Q_{ij}(f_j, f_i), \quad (1)$$

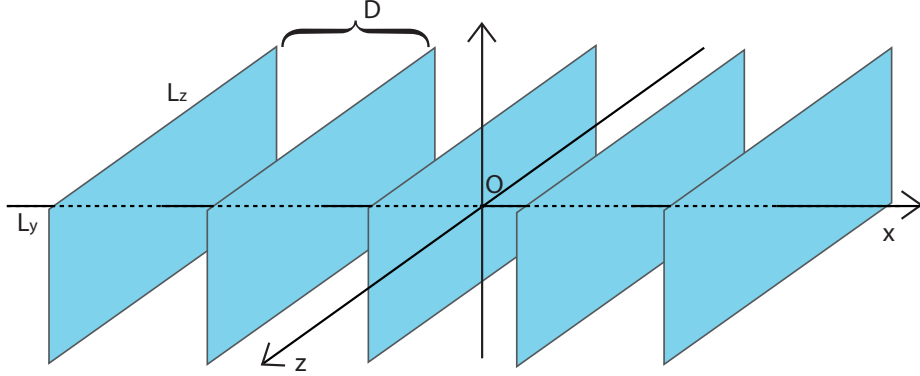


Figure 1: Sketch of array geometry and coordinates system

where the collision integral[3] Q_{ij} , which describes the mechanical interaction between species i and j , has the following expression:

$$Q_{ij}(f_j, f_i) = \frac{1}{2} \left(\frac{\sigma_i + \sigma_j}{2} \right)^2 \int_{S^2} d^2 \hat{\mathbf{k}} \int_{\mathcal{R}^3} d\mathbf{w} [f_j(\mathbf{r}, \mathbf{w}^*|t) f_i(\mathbf{r}, \mathbf{v}^*|t) - f_j(\mathbf{r}, \mathbf{w}|t) f_i(\mathbf{r}, \mathbf{v}|t)] |\mathbf{v}_r \circ \hat{\mathbf{k}}|. \quad (2)$$

In Eq. (1), $f_i(\mathbf{r}, \mathbf{v}|t)$ denotes the distribution function of atomic velocities \mathbf{v} of species i , at spatial location \mathbf{r} and time t . The unit vector $\hat{\mathbf{k}}$ specifies the relative position of two atoms at the time of their impact with relative velocity $\mathbf{v}_r = \mathbf{w} - \mathbf{v}$. The velocities of \mathbf{v}^* and \mathbf{w}^* , which are turned into \mathbf{v} and \mathbf{w} in a restituting collision, are defined as[3]:

$$\mathbf{v}^* = \mathbf{v} + 2 \frac{m_j}{m_i + m_j} (\mathbf{v}_r \circ \hat{\mathbf{k}}) \hat{\mathbf{k}}, \quad (3)$$

$$\mathbf{w}^* = \mathbf{w} - 2 \frac{m_i}{m_i + m_j} (\mathbf{v}_r \circ \hat{\mathbf{k}}) \hat{\mathbf{k}}. \quad (4)$$

Macroscopic quantities associated with the mixture flow are obtained as moments of the the distribution functions. Partial and total number and mass densities are respectively defined as

$$n_i(\mathbf{r}, t) = \int f_i(\mathbf{r}, \mathbf{v}|t) d\mathbf{v}, \quad n(\mathbf{r}, t) = \sum_{i=1}^2 n_i(\mathbf{r}, t) \quad (5)$$

$$\rho_i(\mathbf{r}, t) = m_i n_i(\mathbf{r}, t) \quad \rho(\mathbf{r}, t) = \sum_{i=1}^2 \rho_i(\mathbf{r}, t). \quad (6)$$

The molar fraction, $\chi_i(\mathbf{r}, t)$, of the i -th component and its mass fraction or concentration, $\tilde{\chi}_i(\mathbf{r}, t)$, are defined as

$$\chi_i(\mathbf{r}, t) = \frac{n_i(\mathbf{r}, t)}{n(\mathbf{r}, t)}, \quad (7)$$

$$\tilde{\chi}_i(\mathbf{r}, t) = \frac{\rho_i(\mathbf{r}, t)}{\rho(\mathbf{r}, t)}. \quad (8)$$

Average velocities of each component are then obtained as

$$\mathbf{u}_i(\mathbf{r}, t) = \frac{1}{n_i(\mathbf{r}, t)} \int \mathbf{v} f_i(\mathbf{r}, \mathbf{v}|t) d\mathbf{v}. \quad (9)$$

It is then convenient to define the hydrodynamic velocity, associated with the overall local mixture momentum, as:

$$\mathbf{u}^{hyd}(\mathbf{r}, t) = \frac{\sum_{i=1}^2 \rho_i(\mathbf{r}, t) \mathbf{u}_i(\mathbf{r}, t)}{\rho(\mathbf{r}, t)}. \quad (10)$$

Single component temperature T_i and overall mixture temperature T can be associated with velocity dispersions with respect to the hydrodynamic velocity, as follows:

$$\frac{3}{2} n_i(\mathbf{r}, t) k_B T_i(\mathbf{r}, t) = \frac{1}{2} m_i \int (\mathbf{v} - \mathbf{u}^{hyd})^2 f_i(\mathbf{r}, \mathbf{v}|t) d\mathbf{v}, \quad (11)$$

$$\frac{3}{2} n(\mathbf{r}, t) k_B T(\mathbf{r}, t) = \sum_{i=1}^2 \frac{1}{2} m_i \int (\mathbf{v} - \mathbf{u}^{hyd})^2 f_i(\mathbf{r}, \mathbf{v}|t) d\mathbf{v}. \quad (12)$$

The mixture is set into motion by gas absorption taking place at the surfaces of an infinite array of identical and equally spaced rectangular plates, as sketched in Figure 1. Each plate has negligible thickness and sides of lengths L_y and L_z , respectively. The plates are parallel and their centers lie on a straight line (*array axis*) perpendicular to each plate, being D the distance between two nearest neighbor plate centers. A Cartesian reference frame is constructed by positioning its origin in the center of one of the plates. The x axis coincides with the array axis, whereas the y and z axes are parallel to the plate sides of length L_y and L_z , respectively. The boundary condition, describing the gas mixture behavior at a point \mathbf{r}_p on an absorbing plate surface, is obtained by assuming that atoms of species i impinging on the wall are absorbed with a velocity independent probability α_i or reflected with probability $1 - \alpha_i$. For each species, the distribution functions of reflected atoms is a Maxwellian f_{wi} , defined as:

$$f_{wi}(\mathbf{r}_p, \mathbf{v}|t) = \frac{n_{wi}(\mathbf{r}_p, t)}{(2\pi R_i T_w)^{3/2}} \exp\left(-\frac{\mathbf{v}^2}{2R_i T_w}\right), \quad \mathbf{v} \circ \mathbf{n} > 0 \quad (13)$$

where T_w is the uniform temperature of the plates surface. The gas constants are defined as $R_i = k_B/m_i$, being k_B the Boltzmann constant. The unit vector \mathbf{n} is

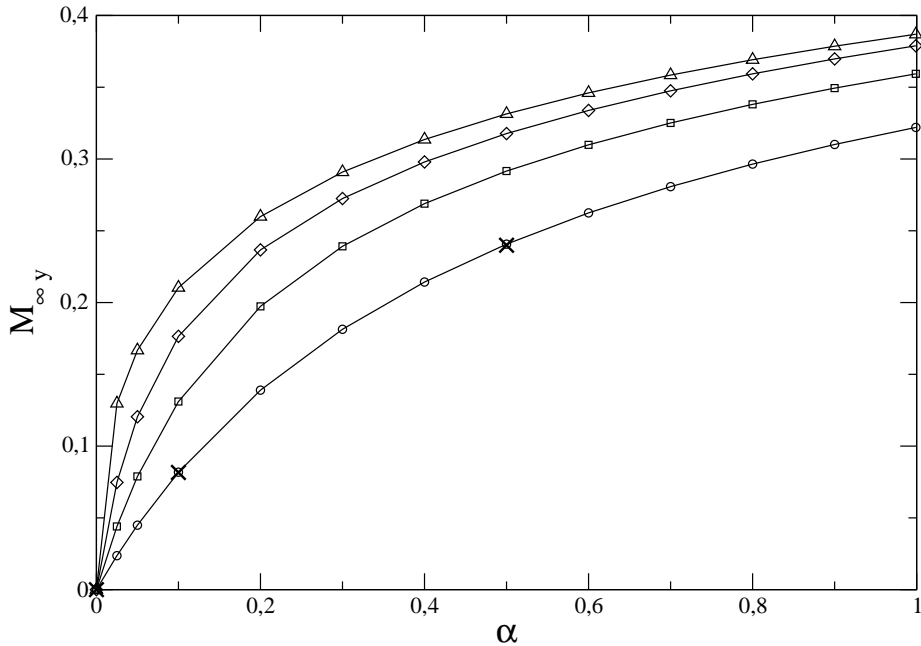


Figure 2: Upstream Mach number, defined by Eq. (24), as a function of absorption probability α and array plates spacing to width ratio, β . \circ : $\beta = 0.4$; \square : $\beta = 0.2$; \diamond : $\beta = 0.1$; \triangle : $\beta = 0.01$; \times : $\beta = 0.4$ DSMC test collisionless flow simulations.

the normal to the plate surface at \mathbf{r}_p , pointing to the gas region. Each amplitude n_{wi} is determined by requiring that the reflected flux equals the impinging flux $-J_i^-$ multiplied by the reflection probability $1 - \alpha_i$:

$$n_{wi} \sqrt{\frac{R_i T_w}{2\pi}} = -(1 - \alpha_i) J_i^-, \quad J_i^- \equiv \int_{\mathbf{v} \circ \mathbf{n} < 0} (\mathbf{v} \circ \mathbf{n}) f_i(\mathbf{r}_p, \mathbf{v}|t) d\mathbf{v}, \quad (14)$$

In order to simplify an otherwise three-dimensional flow, it has been assumed that the length L_z is much greater than the plates width L_y . In this case, it is reasonable to neglect flow gradients along z and to assume f_i to depend on the space variables x and y only. Moreover, if the boundary conditions at infinity are properly set, then the periodic structure of the array will induce a similar periodic structure of the flow field whose calculation can be limited to the strip $\mathcal{S} = \{\mathbf{r} : -\frac{D}{2} \leq x < \frac{D}{2}, y \geq 0\}$. Accordingly, it is assumed that far from the array the mixture is in a state of equilibrium characterized by the following Maxwellian form of the components distribution functions:

$$f_{\infty i}(\mathbf{v}) = \frac{n_{\infty i}}{(2\pi R_i T_{\infty})^{3/2}} \exp \left[-\frac{(\mathbf{v} - \mathbf{u}_{\infty})^2}{2R_i T_{\infty}} \right]. \quad (15)$$

In the expression above, $n_{\infty i}$ is the upstream value of the i -th species number density, whereas T_{∞} and \mathbf{u}_{∞} are the overall mixture upstream temperature and

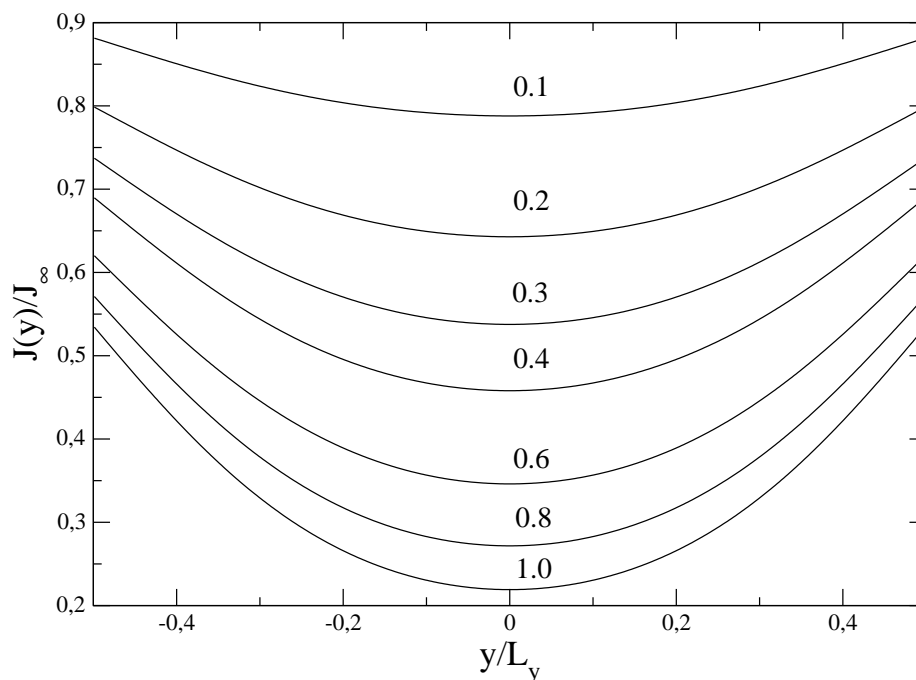


Figure 3: Profiles of normalized incident flux along a plate surface for different values of α . The plates spacing parameter β is set equal to 0.4. Curves are labeled by the corresponding value of α .

bulk velocity, respectively. The bulk velocity \mathbf{u}_∞ is written as

$$\mathbf{u}_\infty = u_{\infty x} \hat{\mathbf{x}} + u_{\infty y} \hat{\mathbf{y}}, \quad (16)$$

being $\hat{\mathbf{x}}$ and $\hat{\mathbf{y}}$ unit vectors respectively parallel and normal to the array axis.

The number of flow parameters and the relationships among them are more easily obtained by the non-dimensional form of the governing equations (1) and the associated boundary conditions (13,14,15). Reference values for mass, length and velocity can be obtained from the equilibrium state at infinity as:

$$m_\infty = \sum_{i=1}^2 \chi_{\infty i} m_i \quad (17)$$

$$\lambda_\infty = \sum_{i=1}^2 \chi_{\infty i} \left(\frac{1}{\sum_{j=1}^2 n_{\infty j} \pi \sigma_{ij}^2 \sqrt{\frac{m_i + m_j}{m_j}}} \right) \quad (18)$$

$$v_\infty = \sqrt{\frac{k_B T_\infty}{m_\infty}} \quad (19)$$

In the above equations, the quantities $\chi_{\infty i}$ are the upstream mixture molar fractions. Eq. (18) defines the mixture mean free path, λ_∞ , being $\sigma_{ij} =$

$(\sigma_i + \sigma_j)/2$ [9]. Adopting the above quantities as new units, readily shows that the solutions of the non-dimensional form of Eqs. (1) depend on the following set of parameters: $Kn = \lambda_\infty/L_y$ (the Knudsen number based on plate width), $\beta = D/L_y$, m_2/m_1 , σ_2/σ_1 , α_1 , α_2 , T_∞/T_w , $\chi_{\infty 1}$, $M_{\infty x}$ and $M_{\infty y}$. The parallel and normal upstream Mach numbers, $M_{\infty x}$ and $M_{\infty y}$, are obtained as the ratio of the corresponding upstream bulk velocity component to the mixture sound speed $c_\infty = \sqrt{\gamma k_B T_\infty/m_\infty}$, being $\gamma = 5/3$ the specific heat ratio of a monatomic gas. The analogy between surface absorption induced flows and vapor condensation flows[1] suggests that not all of the parameters listed above can be freely assigned in stationary conditions. In particular, $M_{\infty y}$, the upstream Mach number associated with the bulk velocity component $u_{\infty y}$, normal to the array axis and related to the net absorption flow, turns out to be a function of the remaining parameters whose values can be assigned arbitrarily.

The large number of problem parameters prevents from obtaining a complete investigation of flow properties. However, physical intuition and a sensible choice of exploratory simulations indicate that some important flow features are not very much dependent on the particular choice of the problem setting. Therefore, the necessarily limited sample of numerical calculations shown below aim at highlighting a few specific aspects of the problem, not at offering a thorough exploration of the flow parameters space.

3. Sketch of the numerical method

Steady numerical solutions of Eqs. (1) have been obtained by the Direct Simulation Monte Carlo (DSMC) method [9]. As is well known, in DSMC the distribution function is represented by a collection of numerical particles whose positions and velocities evolve in time by a sequence of time steps, each of them consisting of a free flight and a local collision sub-step. The former corresponds to the streaming operator at l.h.s. of Eqs. (1), whereas the latter is performed according to stochastic rules, consistent with the structure of the collision terms given by Eq. (2). Macroscopic fluid properties are obtained by averaging particles microscopic states. The method is particularly efficient in steady flows modeling where macroscopic quantities are obtained by time averaging microscopic states after the onset of steady flow conditions.

In the particular DSMC implementation used in the present work, flow properties have been computed in the finite rectangular domain $\mathcal{D} = \{(x, y) \in \mathcal{R}_2 : -\frac{D}{2} \leq x < \frac{D}{2}, |y| < y_{max}\}$, being the outer domain boundaries at $\pm y_{max}$ sufficiently far from the array to ensure the unperturbed flow conditions specified by Eq. (15). The domain is centered on a single absorbing plate which is assigned infinite length L_z and occupies the points of the segment $\mathcal{P} = \{(x, y) \in \mathcal{R}_2 : x = 0, -\frac{L_y}{2} \leq y \leq \frac{L_y}{2}\}$. According to the boundary condition expressed by Eqs. (13,14), whenever a particle of species i hits the plate surface it is absorbed with assigned probability α_i or instantaneously re-emitted with probability $1 - \alpha_i$ in the same spatial position but with new velocity sampled from a probability density proportional to $(\mathbf{v} \circ \mathbf{n})f_{wi}$. Periodic boundary

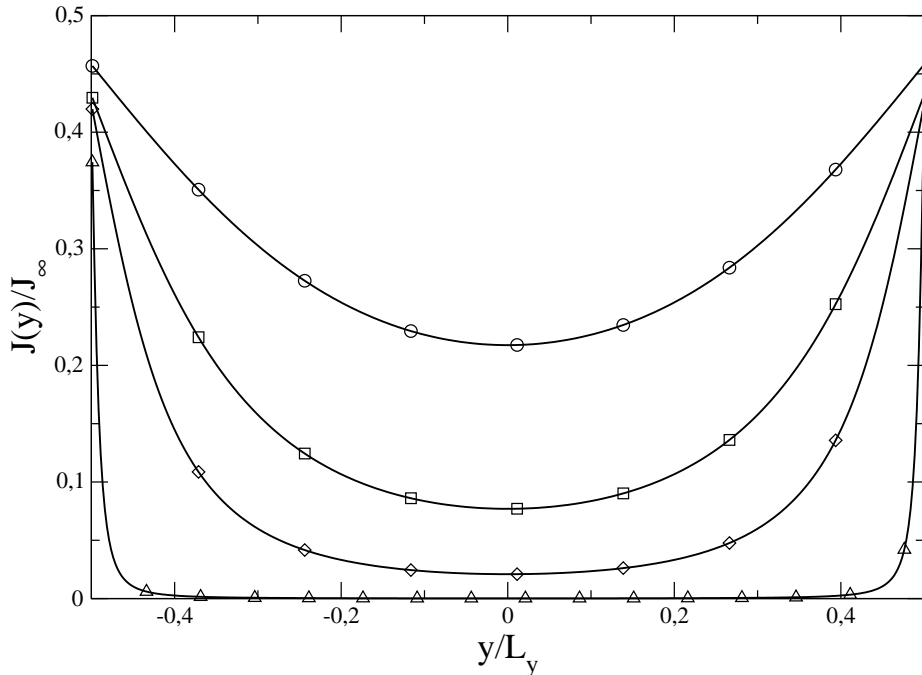


Figure 4: Profiles of normalized incident flux along a plate surface for different values of β . The absorption probability α_i is set equal to 0.8.

conditions are assumed to hold on the sides at $x = \pm \frac{D}{2}$. Hence, when a computational particle crosses any of the two sides parallel to the y , it is re-injected into the domain from the opposite side with the same velocity.

Boundary conditions at open ends at $y = \pm y_{max}$ require special care since the y component of the upstream velocity \mathbf{u}_∞ cannot be prescribed but it is an outcome of the calculation. The problem can be solved by different methods [6]. In the present work the open boundary ends have been replaced by evaporating surfaces which emit atoms of both species into the domain, thus turning the flow into an evaporation/condensation one[4], the array playing the role of condenser. The distribution functions associated with evaporating atoms at $y = \pm y_{max}$ are the Maxwellians:

$$\tilde{f}_{\infty i}(\mathbf{v}) = \frac{\tilde{n}_{\infty i}}{(2\pi R_i \tilde{T}_\infty)^{3/2}} \exp\left[-\frac{\mathbf{v}^2}{2R_i \tilde{T}_\infty}\right]. \quad (20)$$

In Eq. (20) $\tilde{n}_{\infty i}$ and \tilde{T}_∞ are *prescribed* values of species number densities and temperature, not necessarily coinciding with the desired upstream quantities in Eq. (15). If y_{max} is much larger than L_y then the flow field can be divided into three regions. The first one is a one-dimensional Knudsen layer in the vicinity of each evaporating wall. The Knudsen layer is followed by a more or less large

plateau region where the gas is in equilibrium, flowing with uniform density, composition, temperature and velocity towards the array. Finally, the mixture approaches the third region where the array cause macroscopic quantities to have strong variations close to the plates. According to the flow picture outlined above, boundary condition at infinity are set by tuning $\tilde{n}_{\infty i}$ and \tilde{T}_{∞} to obtain the desired reference values of $n_{\infty i}$ and T_{∞} in the equilibrium plateau region, \mathbf{u}_{∞} being a result of the computations. It should be observed that the treatment of the upstream boundary conditions described above and the analogy with evaporation/condensation problems allow obtaining steady *subsonic* flow conditions in the plateau region. Moreover, the extent of the Knudsen layers in the vicinity of the evaporating plates is an increasing function of $M_{\infty y}$ [10, 11], ranging from a few mean free paths for small values of $M_{\infty y}$ to a few hundreds mean free paths when $M_{\infty y}$ is close to unity.

The prescribed boundary conditions produce solutions which are symmetric with respect to the plane $y = 0$ (and even to the plane $x = 0$, if $u_{\infty y} = 0$). Such symmetries have not been exploited to reduce the size of the computational domain in order to increase the number of microscopic samples and obtain flow properties with greater accuracy. Local flow properties have been computed by dividing \mathcal{D} into a grid of non-uniform rectangular cells. Smaller cells (typical size of $\lambda_{\infty}/20$) are used close to the plate surface, whereas cell size is allowed to grow far from the absorbing plate where gradients become negligible. It is to be noted that an accurate description of the Knudsen layers close to evaporating surfaces is not required to build up the algorithm for the control of upstream flow conditions.

4. Collisionless Flow Properties

An important limit case of the general class of flows described by Eqs. (1) is the collisionless or free molecular flow regime, when the gas density is so low that atomic collisions in the gas phase can be neglected. In this case, each species interacts only with the plates of the array and the problem reduces to solving two separate single component steady equations in the form:

$$\mathbf{v} \circ \frac{\partial f_i}{\partial \mathbf{r}} = 0 \quad (21)$$

with boundary conditions at plate surfaces given by Eqs. (13,14). It will be further assumed that atoms coming from the ambient gas surrounding the array do have the following Maxwellian distribution function prior to their first collision with a plate surface:

$$f_{\infty i}(\mathbf{v}) = \frac{n_{\infty i}}{(2\pi R_i T_{\infty})^{3/2}} \exp \left[-\frac{\mathbf{v}^2}{2R_i T_{\infty}} \right]. \quad (22)$$

Since the governing equation and boundary conditions have the same form for both species, the index i may be dropped. The problem described by Eqs. (21)

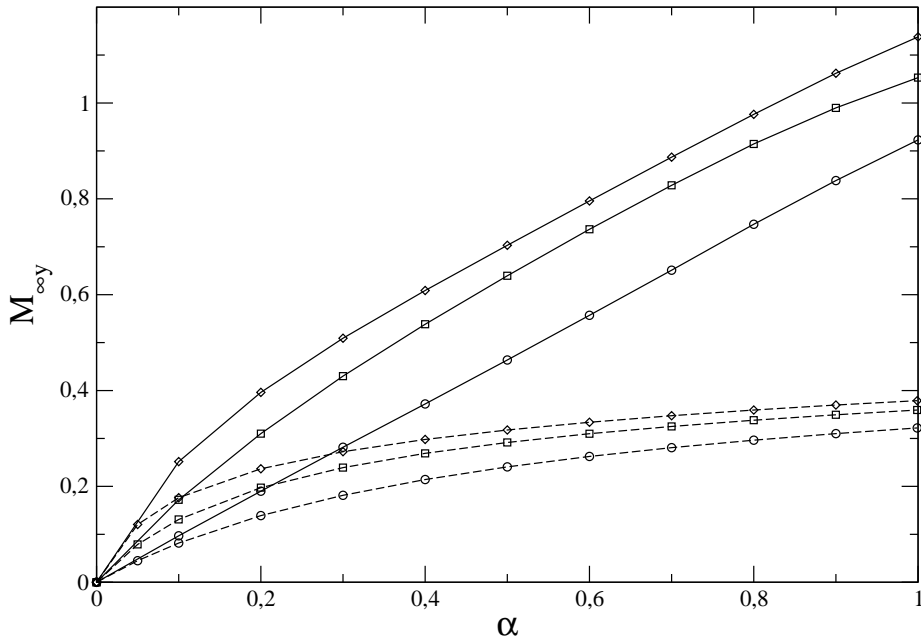


Figure 5: Single component gas. Upstream normal Mach number, $M_{\infty y}$, as a function of α . Solid lines: $Kn = 0.1$, $\beta = 0.1, 0.2, 0.4$, $T_w/T_\infty = 1.0$ and $M_{\infty x} = 0.0$. Dashed lines, free molecular flow regime. \circ : $\beta = 0.4$; \square : $\beta = 0.2$; \diamond : $\beta = 0.1$.

is amenable to analytical treatment by a simple extension of the classical solution methods for free molecular flows[12]. In particular, the determination of both local and global gas absorption rates can be reduced, by straightforward manipulations, to the solution of the following linear integral equation:

$$\tilde{J}(\tilde{y}) = 1 + \frac{\beta^2}{2} \int_{-\frac{1}{2}}^{\frac{1}{2}} \frac{(1-\alpha)\tilde{J}(\tilde{y}') - 1}{\beta^2 + (\tilde{y}' - \tilde{y})} d\tilde{y}' \quad (23)$$

Eq. (23), which applies to both gas components, has a dimensionless form obtained by setting: $\tilde{y} = y/L_y$ and $\tilde{J}(\tilde{y}) = \frac{J^-}{J_\infty}$. The dimensionless incident gaseous flux at position \tilde{y} on one of the plate faces is $\tilde{J}(\tilde{y})$, whereas $J_\infty = n_\infty \sqrt{\frac{RT_\infty}{2\pi}}$ is the reference flux associated with the ambient gas equilibrium state. The dimensionless total absorbed flux is $\tilde{J}_{abs} = \alpha \int_{-\frac{1}{2}}^{\frac{1}{2}} \tilde{J}(\tilde{y}) d\tilde{y}$. It is worth observing that the solutions of Eq. (23) depend on the parameters α and β , not on the temperature ratio T_w/T_∞ . Accurate numerical approximations of $\tilde{J}(z)$ can be obtained by elementary methods. The absorbed flow rate can be converted into an effective flow velocity u_{abs} (or Mach number) by equating J_{abs} to the net flux entering the domain from a rectangular surface element of area D , far from

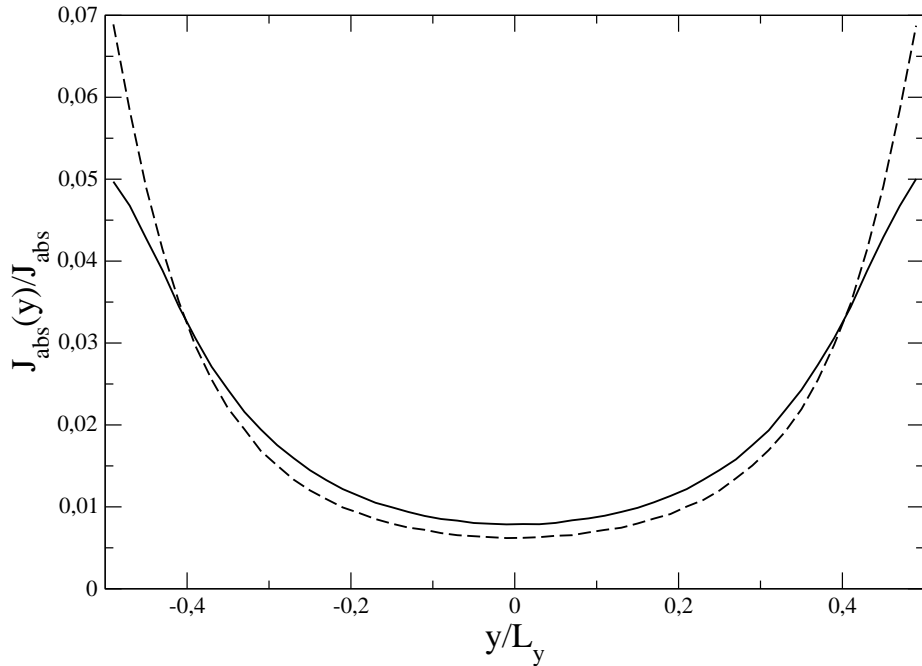


Figure 6: Comparison of local absorption rate profiles along plate surface. Dashed line: free molecular flow, $\beta = 0.1$, $\alpha = 0.5$. Solid line: collisional flow, $Kn = 0.1$, $\beta = 0.1$, $\alpha = 0.5$, $T_w/T_\infty = 1.0$ and $M_{\infty x} = 0.0$.

the array and normal to the y axis:

$$M_{\infty y} = \frac{u_{abs}}{\sqrt{\gamma RT_\infty}} = \frac{1}{\beta \sqrt{2\gamma\pi}} \tilde{J}_{abs} \quad (24)$$

Numerical values of $M_{\infty y}$ have been obtained, as a function of α , for different values of the plate spacing parameter β . As is reasonable, $M_{\infty y}$ is a monotonically increasing function of the absorption probability. However its rate of change is a decreasing function of α since the factor α in \tilde{J}_{abs} is compensated by the reduction of the incident flux caused by the mutual interaction of the opposite faces of two nearest neighbor plates, as shown in Figure 3.

Figure 2 also shows that the increase of $M_{\infty y}$ caused by larger plates packing tends to saturate, particularly at high absorption probabilities. Again, the larger nominal absorption area, obtained by reducing β , is compensated by the interference of nearby plates which allow absorption to occur effectively only on the outermost surface of each plate, as shown in Figure 4

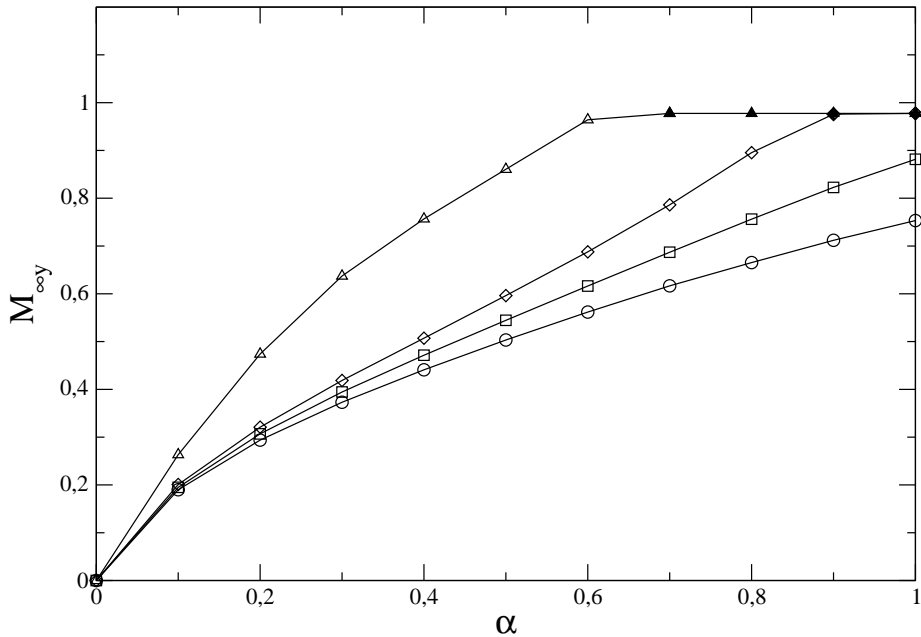


Figure 7: Single component gas. Upstream Mach number as a function of absorption probability and Knudsen number for fixed $\beta = 0.1$, $T_w/T_\infty = 1.0$ and $M_{\infty x} = 0.0$. \circ : $Kn = 0.2$; \square : $Kn = 0.1$; \diamond : $Kn = 0.05$; \triangle : $Kn = 0.005$. Filled symbol mark the (estimated) region of choked flow.

5. Absorption driven flows in the transition regime

5.1. Single component gas flows

The absorption driven flows of a rarefied gas composed by a single species is the second limit case to be examined before discussing the more complex mixture flows. The effect of collisions in the gas phase is now taken into account by solving the full Boltzmann equation for a single species. In this case, solutions are characterized by the following set of free flow parameters: Kn , β , α , T_w/T_∞ and $M_{\infty x}$. Once the above set of quantities is assigned a value, the upstream Mach number $M_{\infty y}$ (i.e. the *net* absorption flow rate) is determined by solving the governing equation.

The results of the simulations presented and discussed in this section aim at providing a few reference cases which allow a better understanding of mixtures flows. In particular, the influence of the Knudsen number $Kn = \lambda_\infty/L_y$, plates spacing ratio β and absorption probability α on $M_{\infty y}$ has been explored. The temperature ratio T_w/T_∞ and the Mach number $M_{\infty x}$, associated with the upstream velocity component parallel to the array axis, have been set equal to one and zero, respectively. Actually, it is reasonable to assume that $M_{\infty y}$ would respond to a variation of T_w/T_∞ as shown in Ref. [1] for the one-dimensional geometry. Similarly, the analogy between the present flow setup and one-dimensional

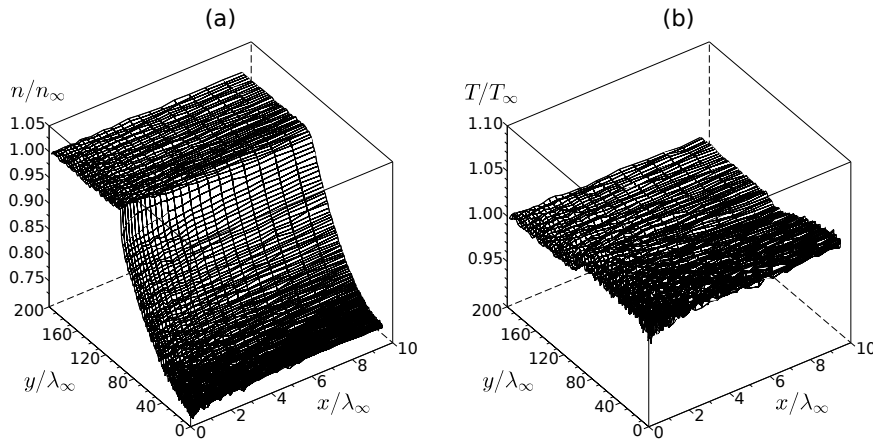


Figure 8: Absorption driven flow of a single component gas, $\alpha = 0.1$, $Kn = 0.005$, $\beta = 0.1$, $T_w/T_\infty = 1.0$, $M_\infty x = 0.0$. **(a)** - Normalized number density field. **(b)** - Normalized temperature field.

condensation flows [6, 1] suggests that the presence of a velocity component parallel to the array axis might have a limited effect on $M_\infty y$. Figure 5 shows the effect of flow parameters α and β on $M_\infty y$, when Kn is set equal to 0.1. Corresponding free molecular flow data are also displayed for easier comparison. For all of three plates spacing considered, the onset of gas advection caused by collisions has a strong effect on absorption rates which are generally higher than companion values in the collisionless regime. Actually, gas phase collisions are expected to increase absorption rates by reflecting towards the array plates molecules that would have escaped absorption in the free molecular flow regime. Moreover, gas convection favors the penetration of molecules in the gap between two nearby plates thus producing flatter absorption profiles, as shown in Figure 6. Transition and free molecular regime data are very close only for low values of α . The explanation can be formulated by the following argument. In the conditions described above the solution of the Boltzmann equation can be expanded in power of α around the value $\alpha = 0$, for which no flow occurs and the solution is the Maxwellian defined by Eq. (22). Hence one may write $f(\mathbf{r}, \mathbf{v}|\alpha) = f_\infty + \alpha \frac{\partial f}{\partial \alpha}|_{\alpha=0} + O(\alpha^2)$. The absorbed flux at any point of an absorbing plate can be written as $\alpha \int_{\mathbf{v} \circ \mathbf{n} < 0} |\mathbf{v} \circ \mathbf{n}| f(\mathbf{r}, \mathbf{v}|\alpha) d\mathbf{v}$. Substituting the expansion for f , it is immediately seen that the transition regime and free molecular flow flux estimates differ at the second order in α .

The effect of the flow parameters Kn and α on $M_\infty y$ is shown in Figure 7 for a fixed plates spacing ratio $\beta = 0.1$. As expected, the increase of absorbing area, caused by the reduction of Kn , generally produces a higher upstream flux. However, the results show that $M_\infty y$ is not always a monotonically increasing

function of α . Below a threshold value of Kn , upstream sonic conditions are attained for a critical value of the absorption probability, $\alpha_c(Kn, \beta)$, less than unity. In these circumstances, a further increase of α does not cause a higher upstream flux, since the flow appears to be choked. For the considered geometry ($\beta = 0.1$), the Knudsen number threshold is around 0.05. As is reasonable, α_c decreases when Kn is reduced, being around 0.9 for $Kn = 0.05$ and close to 0.6 for $Kn = 0.005$. The values of α_c mentioned above have been estimated as the highest α giving rise to nearly sonic uniform flow conditions in well defined upstream plateau regions adjacent to the array.

Absorption probability values higher than α_c lead to flowfields where the evaporation Knudsen layers near the two opposite domain open ends have an extension of a few hundreds mean free paths and merge with the array flow region. In this cases, no well defined upstream equilibrium flow region exists in the domain. In Figure 7, points corresponding to such flow conditions are marked with filled symbols and each α value beyond the estimated α_c is conventionally assigned the slightly subsonic Mach number values associated with α_c . A more detailed description of flowfield structures is given in Figures 8-12 for the smallest value of the Knudsen number, $Kn = 0.005$. The plate spacing parameter is set equal to 0.1. The presented data refer to the two cases $\alpha = 0.1$ and $\alpha = 0.6$. The former corresponds to a relatively slow flow, whereas the latter value produces nearly sonic upstream conditions. In the considered geometric setup, the plates array can be also viewed as a periodic assembly of planar channels with absorbing walls. The gas enters the space between two nearby array plates from the two open ends with equal upstream density and temperature but opposite values of the upstream mean velocity. In absence of an upstream mean velocity component along the array axis, the flow symmetry allows restricting the flowfield representation in the rectangular domain $\{(x, y) \in \mathcal{R}_2) : 0 < x < \frac{D}{2}, 0 < y < y_{max}\}$. The density and temperature fields for $\alpha = 0.1$ are shown in Figures 8(a) and 8(b). The density keeps its upstream value until the gas enters the region delimited by array walls whose absorption causes the density to drop approximately to 70% of its upstream value. It is to be noted that the density gradient along x (normal to array plates) is small. The temperature suffers very small variations from its upstream value, T_∞ . It is possible to observe a slight temperature increase near the plate surface and a slight temperature decrease in the center of channel, near the inlet. The velocity field, separately represented by the x and y components of the gas mean velocity, is depicted in Figures 9(a) and 9(b). The velocity component normal to plates surface, u_x , is very small. It suffers a sudden jump at the channel inlet where the streamlines slightly turn towards the channel center, in response to the small density bump shown in Figure 8(a). However, after a sudden drop, absorption forces u_x to behave roughly as a linear function of x , with little variations along y . The velocity component u_y is spatially uniform before the gas enters the channel region. Wall absorption causes a pressure drop in the space between plates. Accordingly, u_y increases in the channel center and close to the inlet. In the vicinity of the plates surface, the opposite behavior is observed because gas-wall interaction decreases the velocity component parallel to

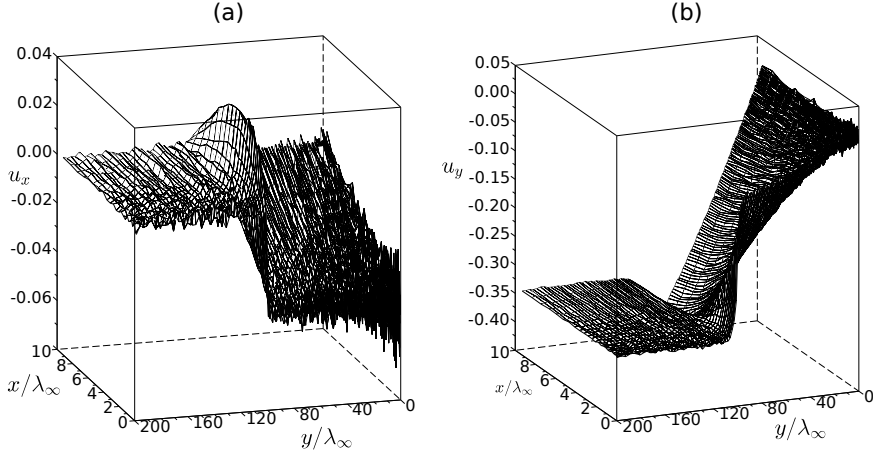


Figure 9: Absorption driven flow of a single component gas, $\alpha = 0.1$, $Kn = 0.005$, $\beta = 0.1$, $T_w/T_\infty = 1.0$, $M_{\infty x} = 0.0$. **(a)** - Map of the gas mean velocity component orthogonal to plates surface, u_x . **(b)** - Map of the gas mean velocity component parallel to plates surface, u_y . Velocity components are normalized to $\sqrt{RT_\infty}$.

plates surface, as expected. On approaching the symmetry plane $y = 0$, where $u_y(x, 0) = 0$, the flow decelerates almost linearly. The flow Mach number map is given in Figure 13(a). As is clear, the flow is everywhere subsonic and the behavior of $M(x, y)$ closely patterns the map of $|u_y(x, y)|$, since $T(x, y) \approx T_\infty$ and $|u_x(x, y)| \ll 1$. When α is increased up to 0.6, the density field, shown in Figure 10(a), is qualitatively similar to the previous one. However, the density drop is much stronger and a slight re-compression is observed near the symmetry plane at $x = 0$. The temperature field, in the companion Figure 10(b), exhibits stronger variations. As expected, the gas temperature increases near the plate where the gas velocity decreases but it decreases rapidly in the central region of the channel inlet following the gas expansion. The subsequent gas re-compression caused by the symmetric counterflow in the second half of the domain, causes the temperature to reach a minimum and increase monotonically till the symmetry plane at $y = 0$.

The behavior of the gas velocity components (see Figure 11) is also very similar to that observed in the case of weaker absorption rate. The magnitude of u_x and u_y is obviously much greater. The Mach number map, shown in Figure 12(b) shows that the unperturbed upstream flow is nearly sonic and that becomes supersonic in the region between two plates.

5.2. Binary gas mixture flows

The mixture flow simulations results discussed below aim at showing the effects of molecular mass ratio, mixture composition and absorption probabilities

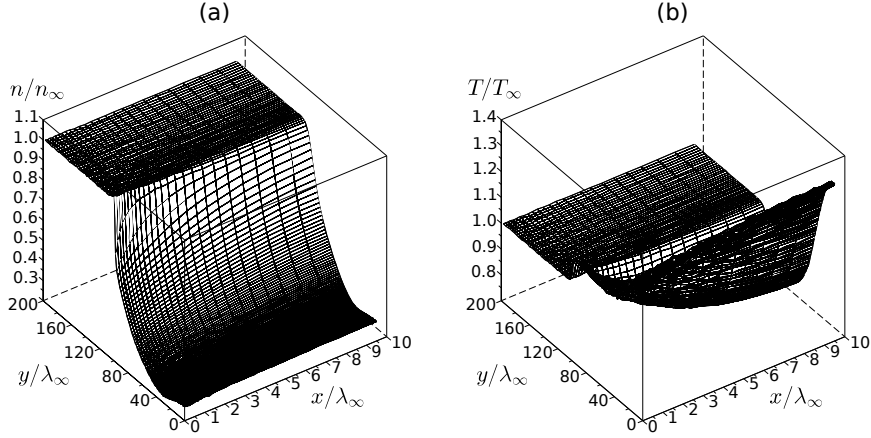


Figure 10: Absorption driven flow of a single component gas, $\alpha = 0.6$, $Kn = 0.005$, $\beta = 0.1$, $T_w/T_\infty = 1.0$, $M_{\infty x} = 0.0$. (a) - Normalized number density map. (b) - Normalized temperature map.

on the net absorption rate. Hence the array geometry has been kept fixed, by setting $Kn = 0.1$ and $\beta = 0.1$. Furthermore, the temperature ratio T_w/T_∞ and the Mach number $M_{\infty x}$ have been set equal to 1.0 and 0.0, respectively. The effect of molecular mass ratio and mixture composition have different effects, depending on the values of the absorption probabilities α_i . Figure 13 presents profiles of $M_{\infty y}$ computed by assigning the same value to the absorption probabilities to the species of a mixture whose mass ratio m_2/m_1 has been set equal to 5. The upstream molar fraction $\chi_{\infty 1}$ has been given the values 0.25, 0.5, 0.75, 0.9783, corresponding to the concentrations $\tilde{\chi}_{\infty 1} = 0.0625, 0.1667, 0.375, 0.90$. In the cases considered, the mixture absorption rates remain rather close to the single species absorption profiles. The deviations are larger than those found in the one-dimensional geometry [1] for similar flow settings and, when considered functions of mixture composition, they exhibit a maximum which seems to be located between $\chi_{\infty 1} = 0.5$ and $\chi_{\infty 1} = 0.75$.

Although the overall mixture absorption rates do not deviate much from the single species case, the different atomic mass values of the two components cause species separation in the vicinity of the array and between the array plates. As a matter of fact, the upstream velocities and temperatures are the same for both species. Hence, the absorption rate per particle is the same for both species. However, the gas-wall collision rates are proportional to $1/\sqrt{m_i}$ therefore equality of absorption rates per particle is obtained by an increase of the concentration of the heavy component in the array region. In principle, the concentrations could depend on both x and y spatial coordinates but in the considered flow conditions the gradient in the direction x , normal to array plates,

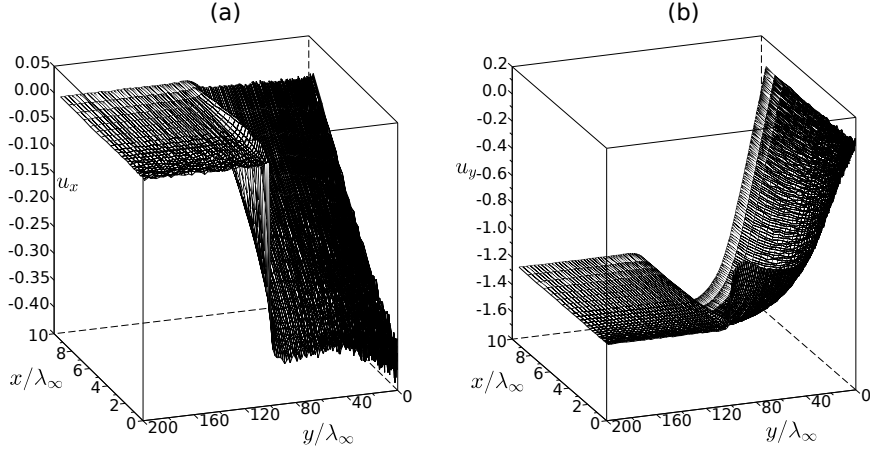


Figure 11: Absorption driven flow of a single component gas, $\alpha = 0.6$, $Kn = 0.005$, $\beta = 0.1$, $T_w/T_\infty = 1.0$, $M_\infty = 0.0$. **(a)** - Map of the gas mean velocity component orthogonal to plates surface, u_x . **(b)** - Map of the gas mean velocity component parallel to plates surface, u_y . Velocity components are normalized to $\sqrt{RT_\infty}$.

is negligible. Figure 14 shows the x -averaged molar concentrations profiles of the light component in the case $\alpha = 0.5$, for three different values of upstream mixture composition. Species separation begins about 10 reference mean free paths from the gap between the plates and reaches its maximum on the flow symmetry plane at $y = 0$, as expected. In the more interesting situation when the wall absorption probabilities of the two mixture components are different, the mixture separation in the vicinity of array plates is determined not only by the mass ratio m_2/m_1 but also by the different values taken by the coefficients α_i . On the ground of previous investigations[7, 1] based on one-dimensional flow geometries, it is expected that the presence of a species with small absorption probability decreases the absorption rate of the most condensible component. The mechanism is very simple: The less condensible species accumulates in front of the absorbing wall thus slowing the absorption process of the other. On the other hand, the absorption rate of the less condensible species is enhanced since the more condensible component behaves as a *shepherd* species which promotes its accumulation near the absorbing wall. In one-dimensional geometry, the effect is quite strong since a small amount of the component with small absorption probability can considerably inhibit the overall mixture absorption rate. However, it is reasonable to expect that the intensity of the effect is influenced by the flow geometry which may affect the accumulation of the less condensible species near the absorbing plates.

In order to investigate this aspect of the problem, a series of DSMC simulations have been performed on a fixed array geometry ($Kn = 0.1$, $\beta = 0.1$) and

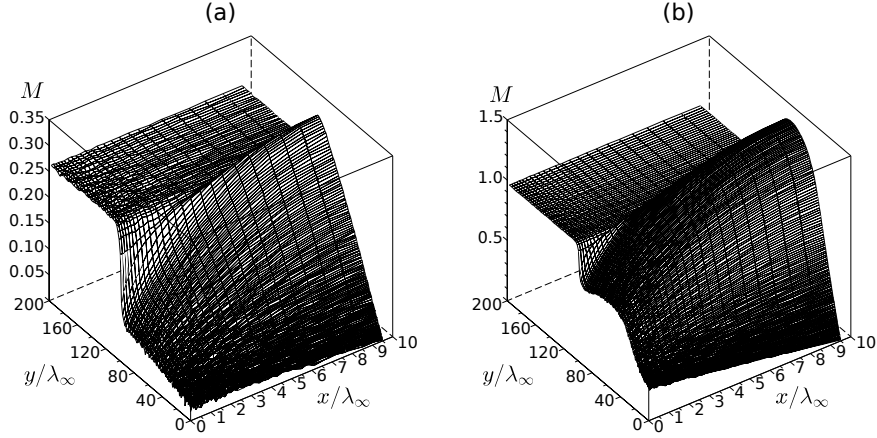


Figure 12: Absorption driven flow of a single component gas, $Kn = 0.005$, $\beta = 0.1$, $T_w/T_\infty = 1.0$, $M_{\infty x} = 0.0$. **(a)** - Mach number field, $\alpha = 0.1$. **(b)** - Mach number field, $\alpha = 0.6$.

setting $T_w/T_\infty = 1.0$, $M_{\infty x} = 0.0$, $m_2/m_1 = 5$, as above. The simulation series consists of three groups. In the first one, species 2 is assigned the role of less condensable species by setting $\alpha_2 = 0.05$; the upstream mixture composition has been varied by setting $\chi_{\infty 2} = 0.1$ ($\tilde{\chi}_{\infty 2} \approx 0.357$) and $\tilde{\chi}_{\infty 2} = 0.1$ ($\chi_{\infty 2} \approx 0.0217$). The second group contains simulations in which the role of less condensable species is played by species 1. Accordingly, α_1 is set equal to 0.05 and the upstream mixture composition varied by setting $\chi_{\infty 1} = 0.1$ ($\tilde{\chi}_{\infty 1} \approx 0.0217$) and $\tilde{\chi}_{\infty 1} = 0.1$ ($\chi_{\infty 1} \approx 0.357$). The third group contains simulations of a mixture of mechanically identical atoms ($m_2 = m_1$) in which the less condensable component is assigned an absorption probability equal to 0.05 and fixed upstream concentration equal to 0.1. The simulations of the third group have been performed to help separating the contributions of mass ratio and absorption probabilities difference to overall mixture absorption rate. In all simulation groups, the absorption probability of the most condensable (and abundant) species, α_m , has been varied between 0.1 and 1.0.

The upstream Mach number curves obtained from the simulations described above are shown in Figure 15 along with the reference curve corresponding to the single component case. The reduction of upstream flow Mach number is evident not only in the two cases where the less condensable species has the higher upstream concentration, but also in the cases where its concentration is quite small. The comparison with the behavior of the mixture of mechanically identical atoms shows that the mass ratio value also plays a role in determining $M_{\infty y}$. The dashed-dotted line and the solid line marked with filled squares respectively refer to two gas mixtures with the same upstream molar composition

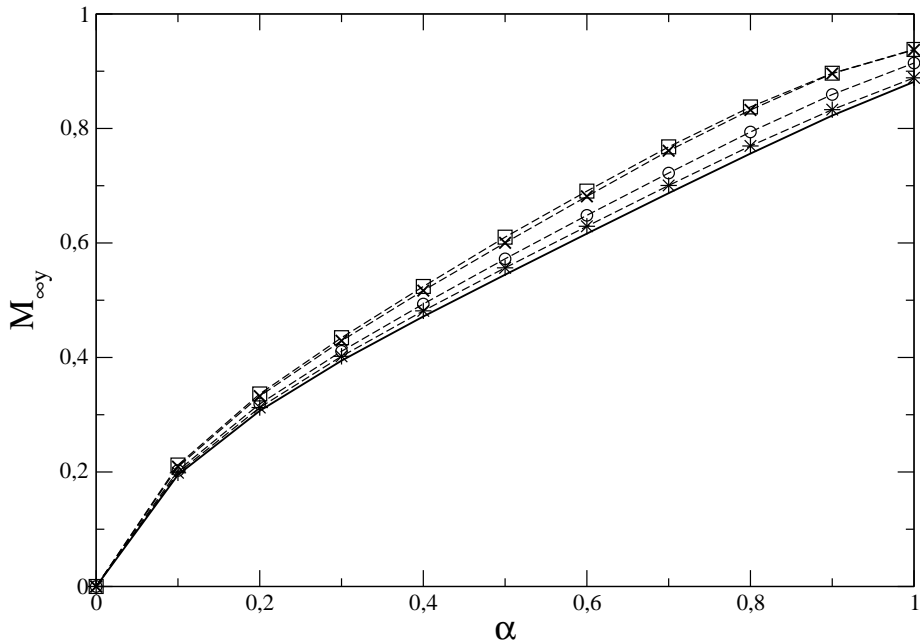


Figure 13: Absorption driven flow of a binary mixture, $Kn = 0.1$, $\beta = 0.1$, $T_w/T_\infty = 1.0$, $M_{\infty x} = 0.0$, $m_2/m_1 = 5$, $\alpha_1 = \alpha_2 = \alpha$. Upstream normal Mach number $M_{\infty y}$ as a function of the absorption probability, α and mixture composition. Solid line: reference single component case; \circ : $\chi_{\infty 1} = 0.25$ ($\tilde{\chi}_{\infty 1} = 0.0625$); \times : $\chi_{\infty 1} = 0.5$ ($\tilde{\chi}_{\infty 1} = 0.1667$); \square : $\chi_{\infty 1} = 0.75$ ($\tilde{\chi}_{\infty 1} = 0.375$); $*$: $\chi_{\infty 1} = 0.9783$ ($\tilde{\chi}_{\infty 1} = 0.90$).

but different mass ratio. In the first case, the two species have equal atomic masses and the presence of the less condensible species is quite effective in decreasing the overall absorption rate, by accumulating in front of the array and within the plates, as shown by the companion concentration curve in Figure 16. In the second case, the mass ratio is 5 and the heavy species is the most abundant one. The overall absorption rate is now higher because the heavy species can more easily penetrate within the gap between the array plates, as seen from the corresponding concentration profile in Figure 16. It is also worth observing that, when the concentration of the less condensible species is small, the Mach number curves are not far from the single component curve. Such results are rather different from those obtained from the one-dimensional problem considered in Ref. [1] where the addition of a small amount of a species with low absorption probability causes large deviations from the absorption rate of a single component gas. The two different behaviors are easily explained by the respective flow geometries. In the one-dimensional absorption driven flow, the mixture is in contact with an infinite planar plate. Flow properties variations are assumed to occur only along the coordinate normal to the plate and the velocity is normal to the plate surface. When one of the mixture components

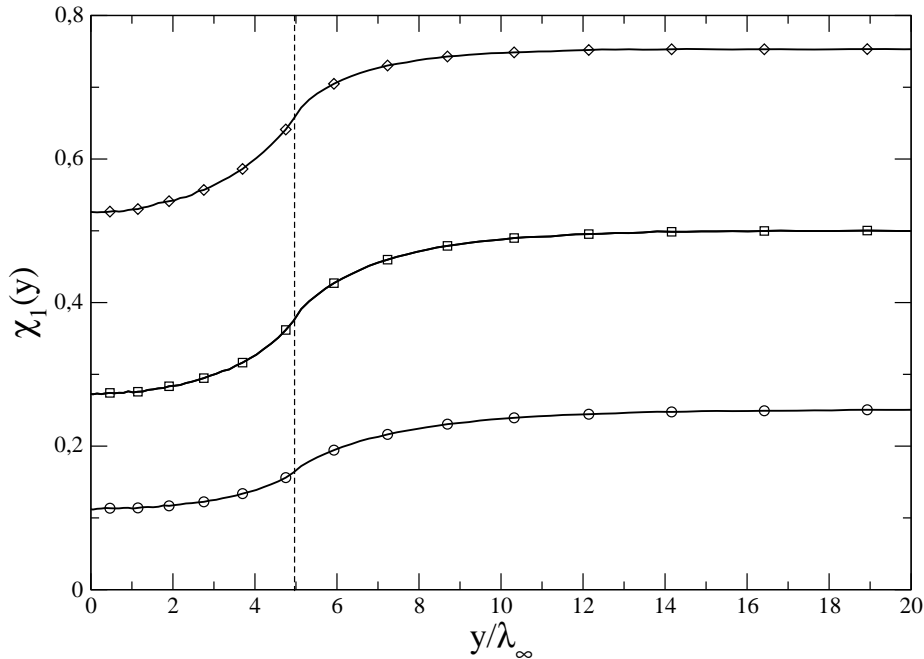


Figure 14: Absorption driven flow of a binary mixture, $Kn = 0.1$, $\beta = 0.1$, $T_w/T_\infty = 1.0$, $M_{\infty x} = 0.0$, $m_2/m_1 = 5$, $\alpha_1 = \alpha_2 = 0.5$, $\chi_{\infty 1} = 0.5$ ($\bar{\chi}_{\infty 1} = 0.1667$). x -averaged molar concentration profiles of the light component. \circ : $\chi_{\infty 1} = 0.25$; \square : $\chi_{\infty 1} = 0.5$; \diamond : $\chi_{\infty 1} = 0.75$. The vertical dashed line marks the right edge of region occupied by array plates.

is weakly absorbed, it accumulates and forms a uniform and almost stationary gaseous sheet above the absorbing surface. The absorption of the second component is reduced just because its atoms have to penetrate the sheet before reaching the wall at the position of minimum concentration.

In the two dimensional case, accumulation of the less condensible component is also present, as shown in Figure 16, but now there exist a velocity component parallel to the plates whose length is finite in y direction. As a result, the concentration of the less condensible species along the plates surface is no longer uniform since it reaches its maximum in on the symmetry plane $y = 0$ but it is closer to its upstream value near the plates edges. Therefore the accumulation of the less condensible species is less effective in reducing the overall mixture absorption.

6. Final remarks and conclusions

Flows of single component and binary gas mixtures generated by absorption at the surface of an infinite array of planar parallel plates have been investigated in the early transition regime by numerical solution of a system of coupled, spatially two-dimensional Boltzmann equations. Single component gas simulations

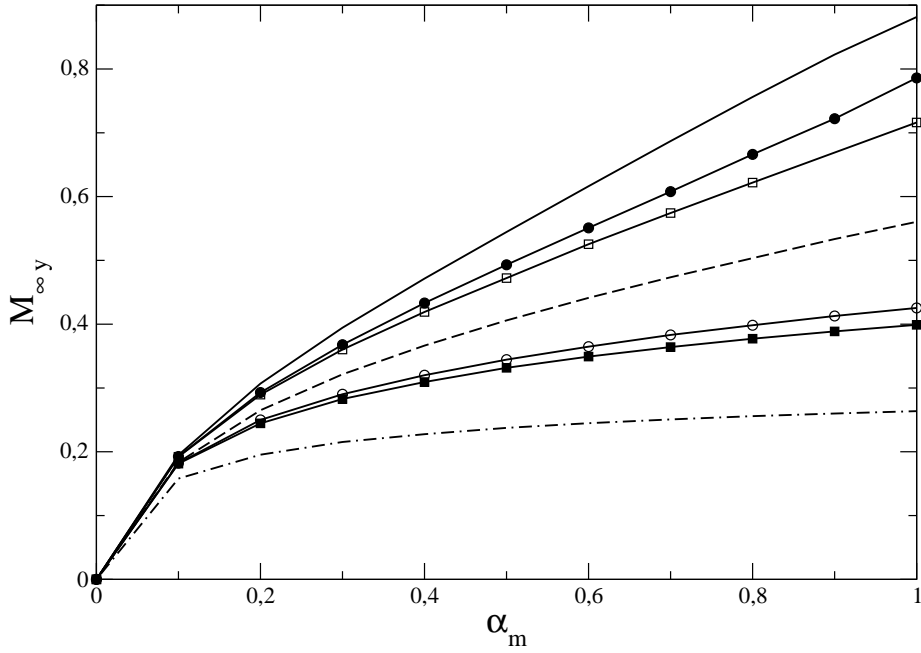


Figure 15: Absorption driven flow of a binary mixture, $Kn = 0.1$, $\beta = 0.1$, $T_w/T_\infty = 1.0$, $M_{\infty x} = 0.0$, $m_2/m_1 = 5$, Overall upstream mixture Mach number $M_{\infty y}$ as function of the absorption probability α_m of the most abundant component. The absorption probability of the less abundant component, α_l , has been kept fixed and equal to 0.05. \circ : $\alpha_2 = \alpha_l$, $\chi_{\infty 2} = 0.1$ ($\tilde{\chi}_{\infty 2} = 0.357$); \square : $\alpha_1 = \alpha_l$, $\chi_{\infty 1} = 0.1$ ($\tilde{\chi}_{\infty 1} = 0.0217$); \bullet : $\alpha_2 = \alpha_l$, $\tilde{\chi}_{\infty 2} = 0.1$ ($\chi_{\infty 2} = 0.0217$); \blacksquare : $\alpha_1 = \alpha_l$, $\tilde{\chi}_{\infty 1} = 0.1$ ($\chi_{\infty 1} = 0.357$); dashed line: $m_2 = m_1$, $\alpha_2 = \alpha_l$, $\chi_{\infty 2} = 0.1$; dashed-dotted line $m_2 = m_1$, $\alpha_2 = \alpha_l$, $\chi_{\infty 2} = 0.357$.

have been performed to investigate the transition from the free molecular to the collisional flow regime and the influence of gas phase collisions on the overall absorption rate. Gas components separation and interaction have been investigated, in particular when one of the gas mixture component is present in small amounts and has a very low absorption probability. The results show that the overall absorption rate in the two-dimensional geometry shows a considerable deviation from the results of a simpler one-dimensional model of the same phenomenon. On the ground of the results obtained so far, it seems reasonable to conclude that accurate modeling of the device geometry would be necessary before planning comparisons with experimental data. Simulations on simplified flow geometries, although useful, are likely to provide only a qualitative picture of the flow properties.

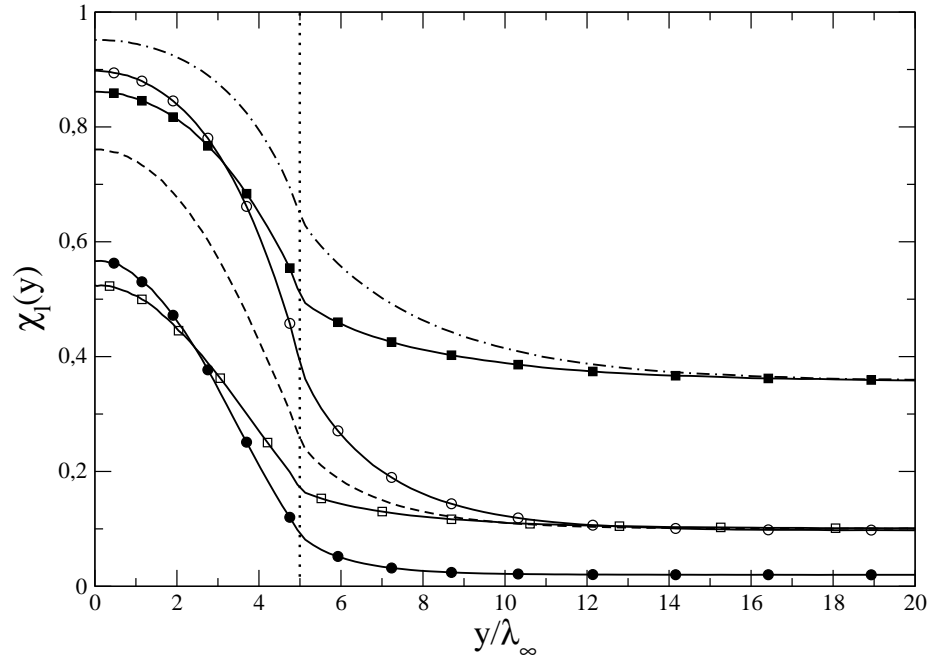


Figure 16: Absorption driven flow of a binary mixture, $Kn = 0.1$, $\beta = 0.1$, $T_w/T_\infty = 1.0$, $M_{\infty x} = 0.0$, $m_2/m_1 = 5$, $\alpha_l = 0.05$, $\alpha_m = 0.5$. x -averaged molar concentration profiles of the less abundant component. Curve markers are the same of Figure 15.

Acknowledgment

The authors gratefully acknowledge the support received from Fondazione Cariplo and SAES Getters within the framework of the projects *Surface interactions in micro/nano devices* and *Mathematical models for active barriers*.

References

- [1] Frezzotti A, Ghiroldi GP, Gibelli L. Rarefied gas mixtures flows driven by surface absorption. *Vacuum* 2012;86(11):1731–8.
- [2] Cercignani C. *The Boltzmann Equation and its Applications*. Berlin: Springer-Verlag; 1988.
- [3] Kaper G, Ferziger JH. *Mathematical Theory of Transport Processes in Gases*. Amsterdam: North-Holland; 1972.
- [4] Sone Y. Kinetic theoretical studies of the half-space problem of evaporation and condensation. *TTSP* 2000;29(3-5):227–60.
- [5] Aoki K, Takata S, Kosuge S. Vapor flows caused by evaporation and condensation on two parallel plane surfaces: Effect of the presence of a non-condensable gas. *Physics of Fluids* 1998;10:1519–33.
- [6] Frezzotti A, Ytrehus T. Kinetic theory study of steady condensation of a polyatomic gas. *Physics of Fluids* 2006;18:027101–.
- [7] Taguchi S, Aoki K, Takata S. Vapor flows condensing at incidence onto a plane condensed phase in the presence of a non-condensable gas. i. subsonic condensation. *Physics of Fluids* 2003;15:689–705.
- [8] Lafferty J, editor. *Foundations of Vacuum Science and Technology*. John Wiley & Sons; 1998.
- [9] Bird GA. *Molecular Gas Dynamics and the Direct Simulation of Gas Flows*. Oxford: Clarendon Press; 1994.
- [10] Ytrehus T. Theory and experiments on gas kinetics in evaporation. In: Potter JL, editor. *Rarefied gas dynamics*; vol. 51 of *Progress in astronautics and aeronautics*. American Institute of Aeronautics and Astronautics; 1977, p. 1197–205.
- [11] Frezzotti A. Kinetic theory description of the evaporation of multi-component substances. In: Shen C, editor. *Rarefied Gas Dynamics, Proceedings of the 20th International Symposium, 19-23 August 1996, Beijing, China*. Beijing, China: Peking University Press; 1997, p. 837–46.
- [12] Kogan MN. *Rarefied Gas Dynamics*. New York: Plenum Press; 1969.